Resolution-Controlled Conductivity Discretization in Electrical Impedance Tomography

R. Winkler

A. Rieder

INSTITUT FÜR WISSENSCHAFTLICHES RECHNEN
UND MATHEMATISCHE MODELLBILDUNG

Anschriften der Verfasser:

Dipl.-Math. techn. Robert Winkler
Institut für Angewandte und Numerische Mathematik
Karlsruher Institut für Technologie (KIT)
D-76128 Karlsruhe

Prof. Dr. Andreas Rieder
Institut für Angewandte und Numerische Mathematik
Karlsruher Institut für Technologie (KIT)
D-76128 Karlsruhe

RESOLUTION-CONTROLLED CONDUCTIVITY DISCRETIZATION IN ELECTRICAL IMPEDANCE TOMOGRAPHY

ROBERT WINKLER AND ANDREAS RIEDER

ABSTRACT. This work contributes to the numerical solution of the inverse problem of determining an isotropic conductivity from boundary measurements, known as Electrical Impedance Tomography. To this end, we first investigate the imaging resolution of the Complete Electrode Model in a circular geometry using analytic solutions of the forward problem and conformal maps. Based on this information we propose a discretization of the conductivity space. Roughly speaking, the resulting conductivity meshes comply with the maximal resolution provided by discrete data with a known noise level. We heuristically extend this approach to domains of arbitrary shape and present its performance under a Newton-type inversion algorithm.

1. BACKGROUND AND MOTIVATION

Electrical impedance tomography (EIT) is an imaging method for determining the electrical conductivity of an object from measurements on its surface. The underlying mathematical model is an elliptic boundary value problem where the Dirichlet data represents the potential on the object surface, the Neumann data represents the normal current flow through the surface and an elliptic PDE models the flow of current inside the object. The coefficient of the PDE is the searched-for conductivity. The evaluation of the Neumann-to-Dirichlet (ND) operator for a given conductivity is called the *forward problem* of EIT. The task in EIT is usually to solve the *inverse conductivity problem* (ICP) of determining the conductivity from the knowledge of the ND operator.

Electrode models and inversion. The pioneering work of Calderón [Cal80] started the investigation of the continuum boundary model, where a complete knowledge of the continuum ND operator is assumed. However in practice, one can only apply currents and measure potentials through finitely many electrodes. As a consequence, the available boundary data is finite-dimensional – the ND map of this discrete model is a matrix. Moreover, due to electrochemical effects and the conducting nature of electrodes, it is impossible to prescribe Neumann data or access Dirichlet data explicitly anywhere at the boundary. Instead, the accurate *Complete Electrode Model* (CEM) [SCI92] described in section 2.2 uses Robin-type boundary conditions to account for these effects.

Analytic properties of electrode models are rare. [LR08] show the injectivity of the Fréchet derivative of the ND map for piecewise polynomial conductivities on a triangulation of the domain for the CEM. The number of electrodes necessary for injectivity is finite, but unknown for any fixed triangulation. [BDGVM12] use a model reduction approach to transform the ICP into the problem of determining the resistors in a network, which is uniquely solvable under certain conditions. However, the reduction approach is theoretically justified for radially symmetric near-constant conductivities only and the boundary model is slightly different from commonly used electrode models.

Stability of the reconstruction scheme is a critical matter for solving the ICP with measured data. Due to Alessandrini's logarithmic stability estimate [Ale88, Theorem 1] in the operator norm of the Dirichlet-to-Neumann (DN) map, the ICP for the continuum model is usually

---

said to be exponentially unstable. Later results (e.g. [Dob92], [Pal02], [MMM04]) show that the stability decays rapidly away from the boundary in typical norms. The consequence of all results is that regularization is necessary to achieve a stable inversion scheme for the ICP. In the absence of a general analytic result, stability studies for electrode models are usually done by investigating what can actually be detected in a fixed domain geometry and electrode setting. Here the notion of *sensitivity* (or *distinguishability* [Isa86], *detectability*), i.e. the effect of perturbations in conductivity to boundary measurements, is important.

Most algorithms for the computation of the ICP are either motivated by the continuum model (for example complex geometrical optics solutions [Nac96], factorization method [BH00]) or regularized iterative methods for an electrode model. An overview can be found in [MS12]. In this work we consider the iterative Newton-type method REGINN for the CEM [LR06]. All numerical inversion methods require a discretization of the problem, in particular of the underlying conductivity space.

Aim and structure of this work. We have pointed out that it is necessary to discretize the conductivity space and to find a suitable regularization scheme when solving the ICP for an electrode model and noisy measurements. While the former is traditionally done by a simple triangulation of the domain, the choice of regularization is delicate as it imposes assumptions on the searched-for conductivity – usually on its smoothness – to control noise amplification during inversion. As a consequence, EIT images are typically heavily blurred.

Our tailored discretization scheme for the conductivity space is piecewise constant on a partition of the domain with a locally adaptive, noise-dependent mesh size which we call an *optimal resolution mesh*. It inherits the smallest possible details which are recoverable from boundary data with a given noise level. Solving the ICP on these meshes with a Newton-type algorithm can be done efficiently with the estimated noise level as the only free design parameter for regularization.

In section 2, we introduce the relevant EIT models and notations. In section 3, we derive an analytic solution for the CEM forward problem on a disk in the presence of a centered circular perturbation in conductivity. Next, we use conformal maps to extend this result to perturbations at arbitrary locations in section 4. We use these analytic solutions to get local resolution information of the CEM. With this information, we design optimal resolution meshes to discretize the conductivity space in section 5. We outline the connections between the CEM and the continuum model and also compare our results to the results of [MMM04] and the meshes arising from resistor networks in [BDGVM12]. We then heuristically extend our results to domains of arbitrary shape. Finally, we demonstrate the performance of these discretizations using the regularized inexact Newton scheme REGINN [Rie99] in section 6.

2. Preliminaries

A *potential* $u \in H^1(\Omega)$ on a source-free, simply connected domain $\Omega \subset \mathbb{R}^2$ with piecewise Lipschitz boundary is a solution of the elliptic equation

$$-\nabla \cdot (\sigma \nabla u) = 0 \quad \text{on} \quad \Omega, \tag{1}$$

where $\sigma \in L^\infty_+(\Omega) = \{\varphi \in L^\infty(\Omega) | \varphi > 0 \text{ a.e.}\}$ is the *isotropic conductivity coefficient*.

2.1. **Continuum boundary model.** For given *Dirichlet* boundary data

$$u|_{\partial\Omega} = f \ \in \ H^{1/2}(\partial\Omega), \tag{2}$$

the problem (1),(2) has a unique solution. Denoting by ν the outer normal on $\partial\Omega$, we call

$$\sigma \frac{\partial u}{\partial \nu} =: i_\nu \ \in \ H^{-1/2}_\diamond(\partial\Omega) = \left\{ \varphi \in H^{-1/2}(\partial\Omega) \, | \langle \varphi, 1 \rangle_{\partial\Omega} = 0 \right\} \tag{3}$$

the corresponding *Neumann* data. Conversely, the problem (1),(3) has a solution which is unique if we require the trace of u to have vanishing mean, that is

$$u|_{\partial\Omega} \in H_\diamond^{1/2}(\partial\Omega) = \left\{\varphi \in H^{1/2}(\partial\Omega) \,|\, \langle\varphi, 1\rangle_{\partial\Omega} = 0\right\}.$$

Hence, the ND operator

$$\Lambda_\sigma \colon H_\diamond^{-1/2}(\partial\Omega) \to H_\diamond^{1/2}(\partial\Omega), \quad i_\nu \mapsto f,$$

and its inverse are well-defined and one-to-one. The ICP in this setting is the inversion of the operator $\sigma \mapsto \Lambda_\sigma$. Uniqueness is shown in [AP06].

2.2. Electrode boundary models.
Electrode boundary models describe the injection of currents and the measurement of potentials through a finite number of electrodes. Assume we have electrodes[1]

$$E_1, \ldots, E_L \subset \partial\Omega, \quad L \in \mathbb{N}_{\geq 2},$$

at which we can inject current patterns $I \in \mathbb{R}_\diamond^L = \left\{V \in \mathbb{R}^L \,|\, \langle V, 1\rangle = 0\right\}$ and measure the resulting potential vectors $U \in \mathbb{R}_\diamond^L$. We assume that normal current i_ν at the domain boundary only occurs at electrodes and that the electrodes are perfect conductors, i.e. the potential is constant on each electrode. Furthermore, we model contact impedances $z_l \geq 0$ that occur at each electrode-domain interface and cause a potential drop $z_l i_\nu$, cf. [SCI92]. This leads to Robin-type boundary conditions

$$(4a) \qquad i_\nu = 0 \qquad\qquad \text{on } \partial\Omega \setminus E, \quad E = E_1 \cup \ldots \cup E_L,$$

$$(4b) \qquad u + z_l i_\nu = U_l \qquad\qquad \text{on } E_l, \quad l = 1, \ldots, L,$$

$$(4c) \qquad \int_{E_l} i_\nu \, \mathrm{d}S = I_l, \qquad\qquad l = 1, \ldots, L.$$

For $z_l \equiv 0$, (1),(4) is called the *Shunt Model*, for $z_l > 0$ it is called *Complete Electrode Model* (CEM). The CEM is usually defined weakly as the unique solution $(u, U) \in H_\diamond^1(\Omega) \times \mathbb{R}_\diamond^L$ of

$$(5) \qquad a\big((u, U), (w, W)\big) = \sum_{l=1}^L I_l W_l \quad \text{for all } (w, W) \in H^1(\Omega) \times \mathbb{R}_\diamond^L,$$

where $a \colon \big(H^1(\Omega) \times \mathbb{R}_\diamond^L\big) \times \big(H^1(\Omega) \times \mathbb{R}_\diamond^L\big) \to \mathbb{R}$,

$$(6) \qquad a\big((v, W), (w, W)\big) = \int_\Omega \sigma\nabla v \cdot \nabla w \, \mathrm{d}x + \sum_{l=1}^L \frac{1}{z_l} \int_{E_l} (v - V_l)(w - W_l) \, \mathrm{d}S,$$

see [SCI92]. We denote the ND (or Current-to-Voltage) map of the CEM by

$$(7) \qquad \Lambda_{\sigma,L} \colon \mathbb{R}_\diamond^L \to \mathbb{R}_\diamond^L, \quad I \mapsto U.$$

The ICP for the discrete setting is the inversion of the operator $\sigma \mapsto \Lambda_{\sigma,L}$ with σ restricted to some subspace of $L_+^\infty(\Omega)$.

2.3. Sensitivity for detecting perturbations.
A keystone in our analysis is the investigation of the sensitivity of measurements to perturbations in conductivity. For $\sigma, \widetilde\sigma \in L_+^\infty(\Omega)$ and considering Λ_σ as an operator on $L^2(\partial\Omega)$, we call

$$(8) \qquad \lambda_{\sigma,\widetilde\sigma} = \frac{\left\|\Lambda_{\sigma,L} - \Lambda_{\widetilde\sigma,L}\right\|_2}{\left\|\Lambda_{\widetilde\sigma,L}\right\|_2} \quad \text{and} \quad \lambda_{\sigma,\widetilde\sigma}^* = \frac{\left\|\Lambda_\sigma - \Lambda_{\widetilde\sigma}\right\|_2}{\left\|\Lambda_{\widetilde\sigma}\right\|_2}$$

---

[1]We identify electrodes with the surface they cover on the domain boundary.

the (relative) *sensitivities* for distinguishing σ from $\widetilde{\sigma}$ by electrode and continuum boundary measurements, respectively. Of special interest is the sensitivity

$$\lambda_\sigma := \lambda_{\sigma,1}$$

for distinguishing a perturbed conductivity $\sigma(x) = 1 + \eta(x)$ from the homogeneous case. Assume that we have a measurement setting with the *relative spectral error bound*

$$(9) \qquad \frac{\|\Lambda_{\mathrm{meas}} - \Lambda_{1,L}\|_2}{\|\Lambda_{1,L}\|_2} \leq \varepsilon, \quad \varepsilon > 0,$$

where Λ_{meas} is a noisy measured ND map of the CEM in the homogeneous case $\sigma \equiv 1$. Then, it is natural to call a perturbation η *detectable* in this setting if $\lambda_\sigma > \varepsilon$. The size $|\mathrm{supp}(\eta)|$ of a perturbation η reaching the resolution limit of the measurement setup, i.e. resulting in $\lambda_\sigma = \varepsilon$, strongly depends on the contrast of the perturbation and its location inside the domain.

Remark: Our definition of sensitivity (8) and spectral error (9) is slightly different from [Isa86, sec. III], where the absolute error $\|\Lambda_\sigma - \Lambda_{\widetilde{\sigma}}\|_2$ is considered. This absolute error is strongly dependent on the underlying background conductivity – and the contact impedance in a corresponding CEM version – and corresponds to an *absolute* spectral measurement noise level, independent of the magnitude of the measured potentials. In contrast, our definition is normalized by the maximum singular value of the ND map, which corresponds to a measurement error relative to the magnitude of the measured potentials when applying normalized currents. It is less sensitive to the underlying background conductivity and the contact impedances.

3. An analytic solution of the CEM forward problem for a centered circular perturbation in conductivity

The forward problem in EIT is usually solved with numerical methods like finite elements. For some basic geometries, analytic solutions exist in terms of Fourier series. We present an analytic method to compute the operator $\Lambda_{\sigma,L}$ of the CEM for a homogeneous disk containing a single centered circular perturbation. That way, we can compute the sensitivity λ_σ for detecting these circular perturbations explicitly. This is achieved by merging and generalizing the ansatz of [SCI92, Appendix 3] for a single centered perturbation with the model of [Dem11]. By extending the CEM to contact impedances that are varying along each electrode in Appendix B, we set stage for exploiting conformal maps and considering perturbations at arbitrary locations in section 4.

Let $\Omega \subset \mathbb{R}^2$ be the unit disk[2] and let, for some $r_0 \in (0, 1)$, the conductivity in polar coordinates be given as

$$\sigma(r, \theta) = \begin{cases} \sigma_0, & 0 \leq r \leq r_0, \\ \sigma_1, & r_0 < r \leq 1. \end{cases}$$

For $i_\nu \in L^2(\partial\Omega)$, the Fourier representations of a Dirichlet-Neumann pair on $\partial\Omega$ are derived in Appendix A.1 as

$$(10a) \qquad f(\theta) = u(1, \theta) = u_0 + \sum_{k=1}^\infty a_k \cos(k\theta) + b_k \sin(k\theta),$$

$$(10b) \qquad i_\nu(\theta) = \sigma_1 \frac{\partial u}{\partial r}(1, \theta) = \sigma_1 \sum_{k=1}^\infty d_k \left(a_k \cos(k\theta) + b_k \sin(k\theta) \right),$$

for some Fourier coefficients $u_0, a_k, b_k \in \mathbb{R}$ and

$$(11) \qquad d_k = k \frac{1 - c_k}{1 + c_k}, \quad c_k = \frac{\sigma_1/\sigma_0 - 1}{\sigma_1/\sigma_0 + 1} r_0^{2k}, \quad k \in \mathbb{N}.$$

---

[2]All calculations can easily be extended to disks of arbitrary radius.

This means that for centered perturbations, the trigonometric functions are eigenfunctions of Λ_σ with eigenvalues $\tau_{\sigma,k} = (\sigma_1 d_k)^{-1}$.

To determine these coefficients for a given electrode potential vector U in the CEM, we generalize the approach of [Dem11, Appendix]. For the CEM and σ smooth near $\partial\Omega$, we have $u|_{\partial\Omega} \in H_\diamond^{3/2-\alpha}(\partial\Omega)$ and $i_\nu \in H_\diamond^{1/2-\alpha}(\partial\Omega)$ for all $\alpha > 0$, see [DHH+12, Remark 1] and the references therein. This guarantees a sufficiently fast decay of the coefficients and a convergence of the above series. Once the Fourier coefficients are known, we compute the resulting current vector I by (4c). These calculations are carried out in Appendix A.2. Note also the remark therein regarding the truncation of the Fourier series for practical computation. Repeating this process for $L-1$ basis vectors $U^{(1)}, \ldots, U^{(L-1)}$ of $\mathbb{R}_\diamond^L$, we obtain the DN map $\Lambda_{\sigma,L}^{-1}$ and we can determine the ND map $\Lambda_{\sigma,L}$ for the perturbed conductivity σ and finally the sensitivity λ_σ by (8).

Clearly, λ_σ depends (nonlinearly) on the conductivities σ_0 and σ_1 and on the radius r_0 of the perturbation. Moreover, the sensitivity is monotonous in the following sense: Let $\eta > 0$ and let

$$(12) \qquad \sigma_B = \sigma_1 + \eta\chi_B, \quad \sigma_D = \sigma_1 + \eta\chi_D, \quad B \subset D \subset \Omega.$$

Then, $\lambda_{\sigma_D,\sigma_1} \geq \lambda_{\sigma_B,\sigma_1}$ which is shown in Appendix C. It is a CEM version of [GIN90, Appendix I]. By the same argument, a similar monotony holds for increasing values of η and fixed perturbation size.

When studying the imaging resolution of EIT settings, it is insightful to know the smallest radius r_0 of a circular perturbation centered about the origin $\mathcal{O}$ inside the unit disk that can be detected from measurements with spectral noise level ε. This can be achieved by determining r_0 such that $\lambda_\sigma = \varepsilon$ for $\sigma = 1 + \eta\chi_{B_{r_0}}(\mathcal{O})$. Due to the above monotonicity, the smallest radius r_0 for conducting perturbations is reached for $\eta \to \infty$.[3]

4. The CEM under conformal mapping

Conformal maps are angle-preserving deformations of the plane. In particular, solutions of the elliptic PDE (1) remain valid in a conformally transformed geometry (see standard literature, e.g. [Neh52, SL91]). Conformal maps have been used for analyzing the continuum boundary model of EIT e.g. in [SYB84]. Using conformal diffeomorphisms on the unit disk, we will compute the ND map of the CEM analytically for circular perturbations at arbitrary locations of the unit disk by reducing the non-centered situation to the centered case of the previous section. This can be done by mapping the disk conformally onto itself such that the non-centered perturbation is centered about the origin, then transforming the CEM boundary description accordingly and solving the forward problem in this transformed setting.

We will show that due to the nature of conformal maps, the resulting ND map agrees with the one of the initial geometry when the boundary settings are transformed accordingly. With this technique, we can determine λ_σ for all circular perturbations inside a disk.

4.1. Conformal mapping of the CEM on the unit disk.

Let w be a conformal diffeomorphism on the unit disk that maps a point $\mathcal{R} = (R, \varphi) \in [0, 1) \times [0, 2\pi)$ to the origin $\mathcal{O}$. For[4] $\mathbb{C} \sim \mathbb{R}^2$, w and its inverse are given (up to rotation) by[5]

$$(13) \qquad z \mapsto w(z) = \frac{e^{-i\varphi}z - R}{1 - Re^{-i\varphi}z} \quad \text{and} \quad y \mapsto w^{-1}(y) = e^{i\varphi}\frac{y + R}{1 + Ry}.$$

---

[3]In our numerical calculations, we set $\eta = 10^6 - 1$.

[4]We switch between polar coordinate notation in $\mathbb{R}^2$ and complex notation, using whatever is more convenient.

[5]The arguments (R, φ) are omitted. They denote the geometric parameters of w and w^{-1} throughout this work.

In particular, a point on the boundary is again mapped to the boundary since

$$(14) \qquad \left| w(e^{i\theta}) \right| = \left| w^{-1}(e^{i\theta}) \right| = 1, \quad \theta \in [0, 2\pi).$$

Our aim is to transform an EIT setting conformally such that a perturbation on a disk $B_{r_Q}(\mathcal{Q})$, $\mathcal{Q} = (Q, \varphi) \in [0, 1) \times [0, 2\pi)$ and $0 < r_Q < 1 - Q$, is mapped by w to a disk $B_{r_0}(\mathcal{O})$ centered about the origin for some $0 < r_0 < 1$. The relations between the perturbation parameters Q and r_Q, the parameter R of the according conformal map w and the radius r_0 are given by

$$(15) \qquad Q = R \frac{1 - r_0^2}{1 - r_0^2 R^2} \quad \text{and} \quad r_Q = r_0 \frac{1 - R^2}{1 - r_0^2 R^2},$$

that is

$$R = \frac{1 + Q^2 - r_Q^2 - \sqrt{(1 + Q^2 - r_Q^2)^2 - 4Q^2}}{2Q} \quad \text{and}$$

$$r_0 = \frac{1 - Q^2 + r_Q^2 - \sqrt{(1 - Q^2 + r_Q^2)^2 - 4r_Q^2}}{2r_Q},$$

which can be seen by plugging $\pm r_0$ into w^{-1}, using the axis of symmetry in direction φ and the fact that w^{-1} maps circles onto circles. Note that $r_0 > r_Q$ and $R > Q$. The action of w is depicted in Figure 1.
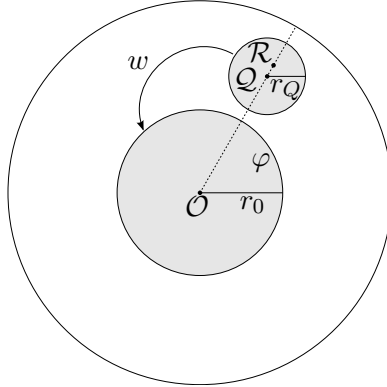

FIGURE 1. The conformal map w maps $B_1(\mathcal{O})$ onto itself, $\mathcal{R}$ to $\mathcal{O}$ and $B_{r_Q}(\mathcal{Q})$ onto $B_{r_0}(\mathcal{O})$.

To parametrize the transformed boundary, let

$$\vartheta := g(\theta) := \arg(w(e^{i\theta})), \quad \theta = g^{-1}(\vartheta) = \arg(w^{-1}(e^{i\vartheta})) \qquad \text{and set}$$

$$w_r := |w|, \quad w_r^{-1} := \left| w^{-1} \right|, \quad w_\theta := \arg(w), \quad w_\vartheta^{-1} := \arg(w^{-1}).$$

Being conformal maps, w and w^{-1} satisfy the Cauchy-Riemann equations. In particular,

$$(16) \qquad \begin{aligned} g'(\theta) &= \left. \frac{\partial w_\theta}{\partial \theta} \right|_{r=1} = \left. \frac{\partial w_r}{\partial r} \right|_{r=1} = \frac{1 - R^2}{1 + R^2 - 2R\cos(\theta - \varphi)} \quad \text{and} \\ (g^{-1})'(\vartheta) &= \left. \frac{\partial w_\vartheta^{-1}}{\partial \vartheta} \right|_{r=1} = \left. \frac{\partial w_r^{-1}}{\partial r} \right|_{r=1} = \frac{1 - R^2}{1 + R^2 + 2R\cos(\vartheta)}. \end{aligned}$$

Moreover, it follows from (14) that

$$0 = \left. \frac{\partial w_r}{\partial \theta} \right|_{r=1} = \left. \frac{\partial w_r^{-1}}{\partial \vartheta} \right|_{r=1} = -\left. \frac{\partial w_\theta}{\partial r} \right|_{r=1} = -\left. \frac{\partial w_\vartheta^{-1}}{\partial r} \right|_{r=1}.$$

When transforming a potential u defined on the unit disk conformally to u^w by $u^w(w(z)) = u(z)$, i.e. $u^w(z) = u(w^{-1}(z))$, the w-transformed Dirichlet data on the unit circle reads

$$f^w(\vartheta) = u^w(1, \vartheta) = u(w^{-1}(1, \vartheta)) = f(g^{-1}(\vartheta)) = f(\theta).$$

For $\sigma \equiv \sigma_1$ near the boundary and using the chain-rule in polar coordinates, the transformed Neumann data reads

$$
\begin{aligned}
i_\nu^w(\vartheta) = {}& \sigma_1 \frac{\partial u^w}{\partial r}(1, \vartheta) \\
= {}& \sigma_1 \frac{\partial u}{\partial r}(w^{-1}(r, \vartheta)) \frac{\partial w_r^{-1}}{\partial r}(r, \vartheta)\bigg|_{r=1} + \sigma_1 \frac{\partial u}{\partial \theta}(w^{-1}(r, \vartheta)) \underbrace{\frac{w_\vartheta^{-1}}{\partial r}(r, \vartheta)\bigg|_{r=1}}_{=0} \\
= {}& \frac{1 - R^2}{1 + R^2 + 2R\cos(\vartheta)} i_\nu(g^{-1}(\vartheta)) = \frac{1 - R^2}{1 + R^2 + 2R\cos(\vartheta)} i_\nu(\theta).
\end{aligned}
$$

(17)

We will now transform the boundary conditions (4) such that the ND map does not change under conformal mapping which is crucial for our further analysis. In particular, the position, width and contact impedance of each electrode change. Condition (4a) states that normal current only occurs on electrode surfaces. For

$$E_l^w := g(E_l),$$

it is obvious that (4a) holds in the transformed setting. Recalling (17), condition (4c) is readily checked as

$$
\begin{aligned}
I_l = {}& \int_{E_l} i_\nu(\theta)\, d\theta = \int_{g(E_l)} i_\nu(g^{-1}(\vartheta)) \left(g^{-1}\right)'(\vartheta)\, d\vartheta \\
= {}& \int_{E_l^w} i_\nu^w(\vartheta) \left(\frac{\partial w_r^{-1}}{\partial r}(r, \vartheta)\bigg|_{r=1}\right)^{-1} \left(g^{-1}\right)'(\vartheta)\, d\vartheta = I_l^w.
\end{aligned}
$$

The last equality holds due to property (16). The transformation of condition (4b) requires a transformation of the contact impedances. We have that

$$
\begin{aligned}
U_l = {}& f(\theta) + z_l i_\nu(\theta) = f(g^{-1}(\vartheta)) + z_l i_\nu(g^{-1}(\vartheta)) \\
= {}& f^w(\vartheta) + z_l \frac{1 + R^2 + 2R\cos(\vartheta)}{1 - R^2} i_\nu^w(\vartheta) \overset{!}{=} f^w(\vartheta) + z_l^w(\vartheta) i_\nu^w(\vartheta) = U_l^w,
\end{aligned}
$$

thus set

(18)
$$z_l^w(\vartheta) := \frac{1 + R^2 + 2R\cos(\vartheta)}{1 - R^2} z_l.$$

The resulting contact impedances are functions of the angular variable ϑ, i.e. they are no longer constant. The CEM in the w-transformed setting giving rise to the same ND map as (4) reads

(19a) $\qquad\qquad i_\nu^w = 0 \qquad\qquad$ on $\partial\Omega \setminus E^w$, $\quad E^w = E_1^w \cup \ldots \cup E_L^w$,

(19b) $\qquad f^w(\vartheta) + z_l^w(\vartheta) i_\nu^w(\vartheta) = U_l \qquad$ on E_l^w, $\quad l = 1, \ldots, L$,

(19c) $\qquad\qquad \int_{E_l^w} i_\nu^w\, dS = I_l, \qquad\qquad\qquad l = 1, \ldots, L.$

For centered circular perturbations, the ND map can again be computed analytically. This is carried out in Appendix B.

Remark: The scaling of the complex plane $z \mapsto \alpha z$, $\alpha > 0$, is a conformal map. The normal current density resulting from a transformed potential is $i_\nu \mapsto \alpha^{-1} i_\nu$. The corresponding boundary settings for preserving the ND map are $E_l \mapsto \alpha E_l$ and $z_l \mapsto \alpha z_l$. Thus, we can consider disks of arbitrary radii.

5. Optimal resolution meshes and approximations

5.1. **Optimal resolution meshes on the unit disk.** With the conformal mapping technique, we are able to determine the sensitivity for detecting circular perturbations anywhere in a disk. With this information, we design a partition of the disk in which perturbations in each cell have roughly the same impact on boundary measurements. To that end, we "fill" the disk with non-overlapping circular cells of fixed sensitivity $\varepsilon > 0$ and apply a Voronoi tessellation afterwards to get a partition of the entire disk. We call the resulting partition an *optimal resolution mesh*.

The generation of such a mesh with approximate sensitivity ε for perturbations of conductivity σ_0 in a background of conductivity σ_1 thus goes in several steps (Algorithm 1):

First, choose a finite set of points $\mathcal{T} \subset B_1(\mathcal{O})$ which are candidates for centers of circular cells. Next, successively pick points $\mathcal{Q}$ from $\mathcal{T}$ and determine the radii r_Q of perturbations centered about $\mathcal{Q}$ and resulting in sensitivity $\lambda_\sigma = \varepsilon$ for $\sigma = \sigma_1 + (\sigma_0 - \sigma_1)\chi_{B_{r_Q}(\mathcal{Q})}$. The radii can be found by a line-search strategy in very few steps since r_Q depends locally quadratic on λ_σ. If $B_{r_Q}(\mathcal{Q})$ lies inside Ω and does not intersect with the previously covered area $\mathcal{C} \subset \Omega$, add $\mathcal{Q}$ to the set of valid points $\mathcal{P}$ and add $B_{r_Q}(\mathcal{Q})$ to the covered area $\mathcal{C}$. Otherwise, discard $\mathcal{Q}$. The result is a union of non-overlapping circles $\mathcal{C}$ with centers $\mathcal{P}$, each resulting in sensitivity $\lambda_\sigma = \varepsilon$ for perturbations of conductivity σ_0 in a homogeneous background medium of conductivity σ_1. Finally, apply a Voronoi tessellation to $\mathcal{P}$ and restrict it to $B_1(\mathcal{O})$ to get a partition of the domain. Results for various values of ε are shown in Figure 2.

Algorithm 1: Generation of an optimal resolution mesh on $\Omega = B_1(\mathcal{O})$

Input: $\varepsilon, \sigma_0, \sigma_1$;
Choose a finite set of test points $\mathcal{T} \subset B_1(\mathcal{O})$;
Set $\mathcal{C} = \emptyset, \mathcal{P} = \emptyset$;
repeat
    Pick a point $\mathcal{Q}$ from $\mathcal{T}$ and set $\mathcal{T} := \mathcal{T} \setminus \mathcal{Q}$;
    Find $r_Q > 0$ such that $\lambda_\sigma = \varepsilon$ for $\sigma = \sigma_1 + (\sigma_0 - \sigma_1)\chi_{B_{r_Q}(\mathcal{Q})}$;
    if $B_{r_Q}(\mathcal{Q}) \subset B_1(0)$ *and* $B_{r_Q}(\mathcal{Q}) \cap \mathcal{C} = \emptyset$ **then**
        Set $\mathcal{P} := \mathcal{P} \cup \mathcal{Q}, \mathcal{C} := \mathcal{C} \cup B_{r_Q}(\mathcal{Q}), \mathcal{T} := \mathcal{T} \setminus B_{r_Q}(\mathcal{Q})$;
    end
until $\mathcal{T} = \emptyset$;
Output: Voronoi tessellation of $\mathcal{P}$, truncated to $B_1(\mathcal{O})$;

Remark: The set $\mathcal{T}$ should be chosen finer than the maximum expected resolution to achieve good results. To avoid big gaps between the circles, it is advisable to pick the innermost point from the set $\mathcal{T}$ first and then successively pick points with the biggest distance to the boundary. A possible choice for $\mathcal{T}$ are points on concentric circles.

5.2. **Comparison with the continuum boundary model.** To compare the resolution achieved by the CEM with the continuum model, we now derive upper bounds for the sizes of perturbations resulting in sensitivity $\lambda_\sigma^* \geq \varepsilon$ in the continuum model.

For a centered circular perturbation inside the unit disk, i.e. $\sigma = \sigma_1 + (\sigma_1 - \sigma_0)\chi_{B_{r_0}(\mathcal{O})}$, the eigenvalues $\tau_{\sigma,k}$ of Λ_σ for the normalized eigenfunctions $\cos(k\cdot)/\sqrt{\pi}$, $\sin(k\cdot)/\sqrt{\pi}$, $k \in \mathbb{N}$, are derived in section 3. In the homogeneous case $\sigma_0 = \sigma_1$, we have $\|\Lambda_{\sigma_1}\|_2 = \sigma_1^{-1}$. For conducting perturbations $\sigma_0 > \sigma_1$, we have $-1 < c_1 < c_2 < \ldots < 0$ in the definition of $\tau_{\sigma,k}$, thus

$$\|(\Lambda_\sigma - \Lambda_{\sigma_1})f_k\|_2 = |\tau_{\sigma,k} - \tau_{\sigma_1,k}|\,\|f_k\| = \left|\frac{1 + c_k}{\sigma_1 k(1 - c_k)} - \frac{1}{\sigma_1 k}\right| = \frac{-2c_k}{\sigma_1 k(1 - c_k)}$$
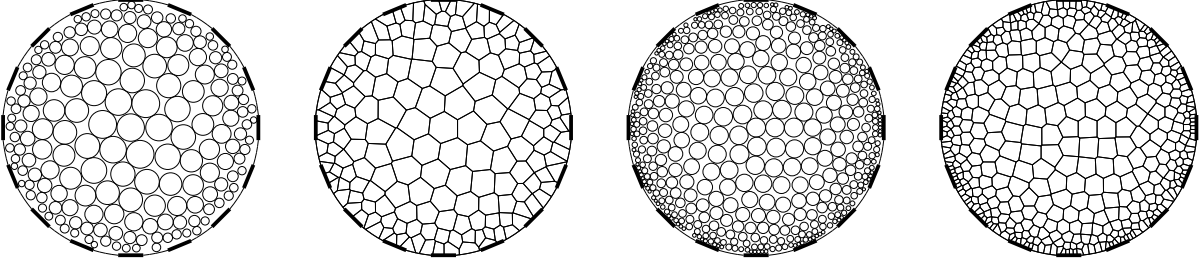
is decreasing in k for eigenfunctions f_k.

FIGURE 2. Circular perturbations and according Voronoi tessellations for $\varepsilon = 0.02$ (left, 182 cells) and $\varepsilon = 0.01$ (right, 445 cells) generated by Algorithm 1. Setting: CEM with 16 equally spaced electrodes that cover 50% of the boundary, $\sigma_1 = 1$, $\sigma_0 = 10^6$ (conducting perturbation) and contact impedances $z_l \equiv 0.01$.

The sensitivity for detecting a centered perturbation is given by

$$\lambda_{\sigma,\sigma_1}^* = \frac{-2c_1}{(1 - c_1)}, \quad c_1 = \frac{\sigma_1/\sigma_0 - 1}{\sigma_1/\sigma_0 + 1} r_0^2.$$

By formally letting $\sigma_0 \to \infty$ for a perfectly conducting inclusion, the radius r_0 resulting in a sensitivity $\lambda_{\sigma,\sigma_1}^* = \varepsilon$ is given as

$$r_0 = \sqrt{\frac{\varepsilon}{2 - \varepsilon}} \quad \text{for} \quad \varepsilon < 1.$$

To investigate the resolution at a point $\mathcal{Q} \in B_1(\Omega)$, we use the conformal map w^{-1} that maps $B_{r_0}(\mathcal{O})$ onto $B_{r_Q}(\mathcal{Q})$ for some $r_Q > 0$. The parameters are given by (15) as

$$(20) \qquad R = R(Q, r_0) = \frac{r_0^2 - 1 + \sqrt{(1 - r_0^2)^2 + 4Q^2 r_0^2}}{2Q r_0^2} \quad \text{and} \quad r_Q = r_0 \frac{1 - R(Q, r_0)^2}{1 - r_0^2 R(Q, r_0)^2}.$$

By (16), the Dirichlet data f_k and the corresponding normal current $i_{\nu,k}$ are transformed to

$$f_k^{w^{-1}}(\theta) = f_k(g(\theta)) \quad \text{and} \quad i_{\nu,k}^{w^{-1}}(\theta) = \frac{1 - R(Q, r_0)^2}{1 + R(Q, r_0)^2 - 2R(Q, r_0)\cos(\theta - \vartheta)} i_{\nu,k}(g(\theta)).$$

Denote by σ_w the w^{-1}-transformed conductivity. Although we do not know the singular system of Λ_{σ_w} explicitly, we can get a lower bound for $\lambda_{\sigma_w,\sigma_1}^*$ by setting $k = 1$, using the conformal mapping properties $\Lambda_{\sigma_w} i_{\nu,1}^{w^{-1}} = \tau_{\sigma,1} f_1^{w^{-1}}$ and $\Lambda_{\sigma_1} i_{\nu,1}^{w^{-1}} = \tau_{\sigma_1,1} f_1^{w^{-1}}$ and using the functions $f_1^{w^{-1}}$ and $i_{\nu,1}^{w^{-1}}$ in (8). This leads to

$$\lambda_{\sigma_w,\sigma_1}^* \geq \frac{\left\| (\Lambda_{\sigma_w} - \Lambda_{\sigma_1}) i_{\nu,1}^{w^{-1}} \right\|_2}{\|\Lambda_{\sigma_1}\|_2 \left\| i_{\nu,1}^{w^{-1}} \right\|_2} = \frac{|\tau_{\sigma,1} - \tau_{\sigma_1,1}|}{\sigma_1} \frac{\left\| f_1^{w^{-1}} \right\|_2}{\left\| i_{\nu,1}^{w^{-1}} \right\|_2} = \alpha_w \lambda_{\sigma,\sigma_1}^*, \quad \text{where} \quad \alpha_w = \frac{\left\| f_1^{w^{-1}} \right\|_2}{\left\| i_{\nu,1}^{w^{-1}} \right\|_2}.$$

Thus to find the radius r_Q resulting in $\lambda_{\sigma_w,\sigma_1}^* \geq \varepsilon = \alpha_w \lambda_{\sigma,\sigma_1}^*$ in the perfectly conducting case, we need to solve the implicit equation

$$r_0 = \sqrt{\frac{\alpha_w^{-1}\varepsilon}{2 - \alpha_w^{-1}\varepsilon}}.$$

It is implicit because the parameter R of the conformal map w^{-1} and thus α_w depend on r_0. However for $\alpha_w^{-1}\varepsilon \ll 1$, r_0^2 depends almost linearly on ε and the solution can be found quickly by the fixed-point iteration

$$r_{0,k+1} = \sqrt{\frac{\alpha_{w_k}^{-1}\varepsilon}{2 - \alpha_{w_k}^{-1}\varepsilon}}, \quad r_{0,0} = \sqrt{\frac{\varepsilon}{2 - \varepsilon}},$$

where w_k^{-1} is the conformal map with parameter $R = R(Q, r_{0,k})$. Once r_0 is found, we can explicitly compute $A_Q = \pi r_Q^2$, an upper bound for the size of a perfectly conducting perturbation centered about $\mathcal{Q}$ and resulting in sensitivity $\lambda^*_{\sigma_w, \sigma_1} \geq \varepsilon$. In particular for $f_1 = \cos(\cdot)/\sqrt{\pi}$, $A_Q \to 0$ as $Q \to 1$ which is shown in Figure 3.

Figures 3a–d show A_Q as a function of Q for a fixed sensitivity in the continuum model ($\lambda^*_\sigma = 0.015$) and in various CEM settings[6] ($\lambda_\sigma = 0.015$) with background conductivity $\sigma_1 = 1$. While the perturbation size A_Q gets arbitrarily small near the boundary for the continuum model, it is bounded away from 0 for the CEM because the concentration of Neumann data near a point is limited by the distance and size of the electrodes. We observe that increasing the number of electrodes does not necessarily increase the resolution inside the disk (a). A decrease of the contact impedances increases the resolution at the center (b). A decrease of the electrode sizes increases the resolution near an electrode, but decreases the resolution at the center (c). A comparison of different types of resistive and conducting perturbations, along with the the results of [MMM04] (see section 5.3), is shown in (d).

It is worth mentioning that perfectly conducting (■ in 3d) and isolating (▼) perturbations result in roughly the same resolution. The resolution of low-contrast conducting perturbations (●) is significantly worse, but it is roughly proportional to the high-contrast case throughout the domain[7]. This means that optimal resolution meshes designed for perfectly conducting or resistive perturbations remain proper choices for reconstructing perturbations with lower contrast since the sensitivity of each perturbation to boundary measurements remains roughly constant. We will make use of this observation by performing all reconstructions on meshes designed for perfectly conducting perturbations in section 6.

Figure 4 shows A_Q as a function of the sensitivities λ_σ (CEM) and λ^*_σ (continuum model) at two locations: the center of the unit disk ($Q = 0$) and a point near the boundary ($Q = 0.95$), centered about an electrode in the CEM. In both cases, A_Q depends almost linearly on the sensitivity. This means that A_Q for unknown sensitivities in the CEM can be approximated very well by linear interpolation/extrapolation of known values.

5.3. **Comparison with results of MacMillan et al.** [MMM04] investigate the detectability of perturbations in conductivity from a finite set of Neumann data for the continuum boundary model. The central result of [MMM04] (cf. Corollary 2.5 and section 2.3.2. therein) is an estimate of the form

$$(21) \qquad \|\Lambda_\sigma i_\nu - f\|_{H^{1/2}(\partial\Omega)} + \epsilon \geq \sup_{i_1, i_2 \neq 0} \frac{C \left| \int_\Omega (\sigma - \widetilde{\sigma}) \nabla u_1 \cdot \nabla u_2 \, dx \right|}{\|i_1\|_{H^{-1/2}(\partial\Omega)} \|i_2\|_{H^{-1/2}(\partial\Omega)}}, \; i_\nu \in \mathcal{I}, \; C = \max_{z \in \Omega} \frac{\sigma(z)}{\widetilde{\sigma}(z)},$$

where $\mathcal{I} \subset H_\diamond^{-1/2}(\partial\Omega)$ is a given finite set of Neumann data, $f = \Lambda_{\widetilde{\sigma}} i_\nu + \epsilon_n$ is noisy Dirichlet data, u_1 and u_2 are solutions of (1),(3) for conductivity σ and Neumann data $i_1, i_2 \in H_\diamond^{-1/2}(\partial\Omega)$ and $\epsilon = \epsilon(\epsilon_n, i_\nu)$ is an error term depending on the measurement error ϵ_n and the non-optimality of i_ν for distinguishing σ from $\widetilde{\sigma}$. Given a fixed $\epsilon > 0$, they generate meshes in [MMM04, section 2.3.2.] (called *graded grids* therein) by finding the sizes $A_\eta = |\text{supp}(\eta)|$ of local perturbations $\eta = \sigma - \widetilde{\sigma}$ such that

$$(22) \qquad \sup_{i_1, i_2 \neq 0} C \left| \int_{\text{supp}(\eta)} \eta \nabla u_1 \cdot \nabla u_2 \, dx \right| \|i_1\|_{H^{-1/2}(\partial\Omega)}^{-1} \|i_2\|_{H^{-1/2}(\partial\Omega)}^{-1} = \epsilon.$$

To compare the radial resolution of the graded grids with our results, we plot A_η versus the location of the center of supp(η) in Figure 3a (marked with asterisks). Lacking an explicit formula, the information was obtained from the left grid of [MMM04, Fig. 3.1], where $\epsilon = 0.1$

---

[6]The angle φ of the point $\mathcal{Q} = (Q, \varphi)$ is fixed such that $\mathcal{Q}$ approaches the center of an electrode as $Q \to 1$ in the CEM.
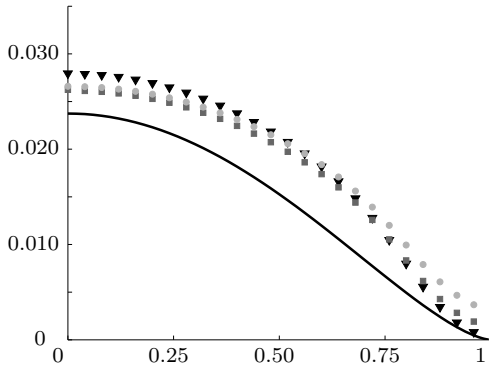
[7]In our computations shown in Figure 3d, the ratios between the areas resolved for $\sigma_0 = 10^6$ and $\sigma_0 = 2$ range from 0.331 to 0.345 throughout the domain.
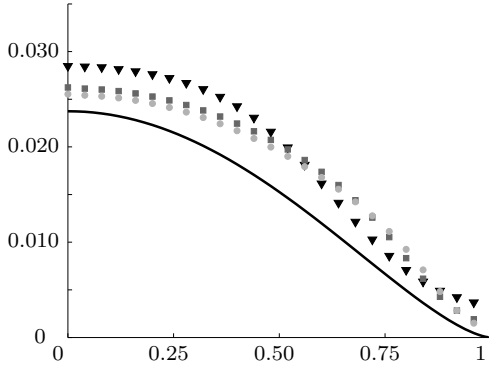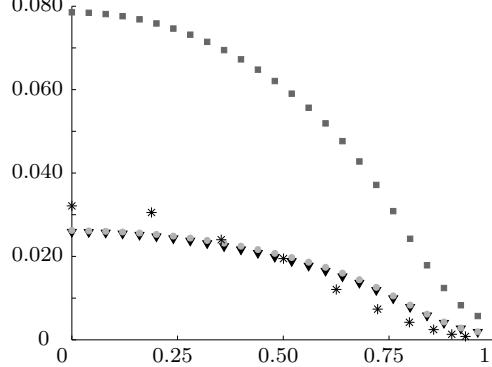
(a) $Q \mapsto A_Q$ plot for $\lambda_\sigma^* = 0.015$ (solid line) and for $\lambda_\sigma = 0.015$ in the CEM with 8 (▼), 16 (■) and 24 (•) electrodes.
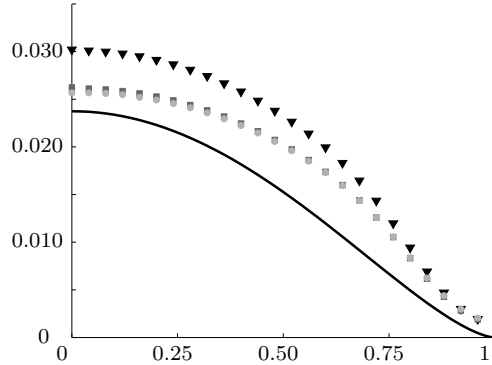
(b) $Q \mapsto A_Q$ plot for $\lambda_\sigma^* = 0.015$ (solid line) and for $\lambda_\sigma = 0.015$ and for 16 electrodes with $z_l \equiv 10^{-1}$ (▼), $z_l \equiv 10^{-2}$ (■) and $z_l \equiv 10^{-3}$ (•).

(c) $Q \mapsto A_Q$ plot for $\lambda_\sigma^* = 0.015$ (solid line) and for $\lambda_\sigma = 0.015$ and 16 electrodes covering 25% (▼), 50% (■) and 75% (•) of the boundary.

(d) $Q \mapsto A_Q$ plot for $\lambda_\sigma = 0.015$ in the CEM for isolating ($\sigma_0 = 10^{-6}$, ▼), conducting ($\sigma_0 = 2$, ■) and perfectly conducting ($\sigma_0 = 10^6$, •) perturbations. The asterisks mark segment sizes of [MMM04, Fig. 3.1] satisfying (22) for $\epsilon = 0.1$ and $\max |\eta| = 1$.

FIGURE 3. Resolved details of the continuum boundary model and the CEM for various settings. CEM parameters as in Figure 2 if not stated otherwise.
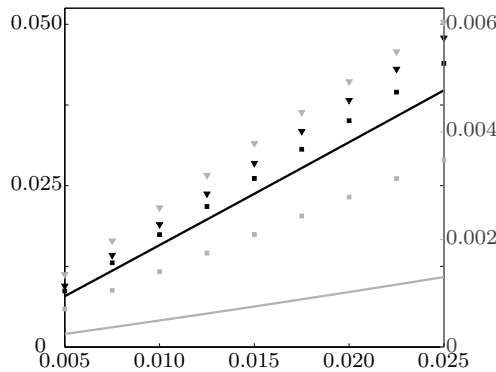
FIGURE 4. $\lambda_\sigma^* \mapsto A_Q$ plot (solid lines) and $\lambda_\sigma \mapsto A_Q$ plot for 8 (▼,▽) and 16 (■,□) electrodes for a conducting ($\sigma_0 = 10^6$) perturbation at the center of a disk ($Q = 0$, black, left ordinate) and near the boundary ($Q = 0.95$, gray, right ordinate).

and $\max |\eta| = 1$ are considered. The perturbation sizes for a fixed ϵ, although not identical to our solutions of section 5.2, show similar characteristics towards the boundary.

5.4. **Comparison with results of a resistor network approach.** The conductivity discretizations in [BDGVM12] arise from a model reduction approach of EIT to the problem of determining the resistors in a linear network [CM00]. The geometry of the discretization is derived from the geometry of the resistor network which has a spiderweb structure with radial beams and concentric rings. This geometry, while theoretically justified for near-constant radially symmetric conductivities, has the disadvantage that the number of cells in each concentric ring is constant. Thus, even though the ring segments get longer towards the center, the resolution in angular direction gets very high at the center as the number of electrodes increases. This is not in accordance with the loss of resolution away from the boundary. Hence the model gets unstable and sensitive to noise when increasing the number of electrodes. Figure 5 shows conductivity discretizations resulting from resistor networks with 13 and 25 electrodes.
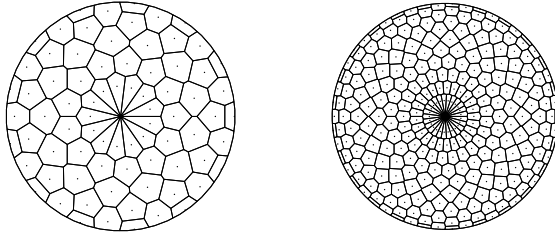

FIGURE 5. Voronoi tessellations resulting from resistor networks with 13 (left) and 25 (right) boundary nodes. The resistor locations (marked with dots) were obtained from the data in [BDGVM12, Fig. 8 and Fig. 3]. The radial resolution near the center is coarse, however the angular resolution is fine due to the fixed number of resistors in each layer.

5.5. **Approximations for domains with arbitrary boundary.** Most EIT applications involve non-circular object geometries. Even in medical applications, where e.g. the cross-section of a human torso is close to an ellipse, using a circular geometry for inversion introduces heavy artifacts which make it impossible to reconstruct anything meaningful if the geometry is not adjusted properly (cf. [DHSS13]). Unfortunately, analytic expressions of conformal maps and their normal derivatives from arbitrary simply connected domains to the unit disk are usually not available. Moreover, the computation of optimal resolution meshes is impractical[8] as it involves the solution of many linear systems of equations with large dense coefficient matrices. Thus, we aim to derive a scheme for quickly generating approximations to optimal resolution meshes on arbitrary domains, motivated by the analytic results of section 5.2. There we observed that the sensitivities for detecting perturbations in the continuum model and the CEM are similar, but the resolution of details in the CEM is limited near the boundary (cf. Figure 3).

The idea is now to use the continuum solution r_Q from (20) as an approximation for the CEM on arbitrary domains, replacing the radial coordinate Q of a point z therein by

$$Q_z = 1 - d(z), \quad z \in \Omega, \quad \text{where} \quad d(z) = \frac{\min\limits_{l=1,\ldots,L} \text{dist}(z, E_l)}{\max\limits_{\zeta \in \Omega} \min\limits_{l=1,\ldots,L} \text{dist}(\zeta, E_l)}$$

is the relative distance of z to the closest electrode.

Inspecting Figures 3a–c, we note that the resolution of the continuum model and the CEM have a similar characteristic, but the CEM curve is offset by the model differences and by the limited resolution near the boundary. To account for these differences in our approximation,

---

[8]The computation of the meshes shown in Figure 2 involved several thousand LU decompositions with up to 30 000 unknowns each and took several days ($\varepsilon = 0.02$) to several weeks ($\varepsilon = 0.01$) in our MATLAB implementation on a 2.2 GHz workstation with 16 CPU cores and 128 GB RAM.

we add a linear correction to the continuum solution r_{Q_z} which "shifts" the resolution curve to match the CEM results at the center and near the boundary. The linearly corrected resolution ρ should satisfy $\rho(z_1) = p_1$ and $\rho(z_2) = p_2$, where z_1 and z_2 are two points at which the radii p_1 and p_2 of resolved details of a given setting are known or can be estimated. The corrected formula reads

$$(23) \qquad \rho(z) := r_{Q_z} + \frac{\Delta p_2 - \Delta p_1}{Q_{z_2} - Q_{z_1}} \left(Q_z - Q_{z_1}\right) + \Delta p_1,$$

where $\Delta p_1 = p_1 - r_{Q_{z_1}}$ and $\Delta p_2 = p_2 - r_{Q_{z_2}}$ are the differences between the given setting and the continuum model at z_1 and z_2, respectively.

By (23), adaptive approximations of the optimal resolution meshes can be created with Algorithm 1, replacing $B_1(\mathcal{O})$ by Ω therein and setting $r = \rho(z)$ for each test point $z \in \mathcal{T}$. We will refer to these adaptive approximations as *adaptive meshes*. Generating an adaptive mesh that way usually takes less than one second in MATLAB on an Intel i7 notebook. For our implementations, we use the data from the circular case at $z_1 = \mathcal{O}$ and $z_2 = (0.95, 0)$ marked with ■ and ▨ in Figure 4, i.e. $Q_{z_1} = 0$ and $Q_{z_2} = 0.95$, and interpolate/extrapolate accordingly for a given sensitivity ε to obtain the values p_1 and p_2. Figure 6 shows resulting adaptive meshes for $\varepsilon = 0.02$ and different geometries.
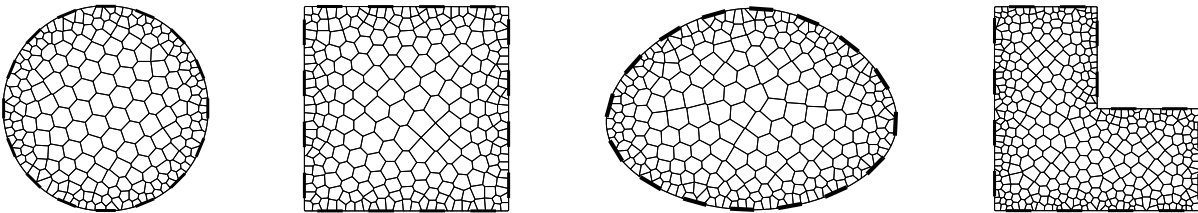

FIGURE 6. Adaptive approximations of optimal resolution meshes in different geometries with 16 electrodes for $\varepsilon = 0.02$.

5.6. **Dynamic mesh size for iterative inversion algorithms.** Iterative Newton-type algorithms successively solve forward problems and apply Newton updates to the searched-for conductivity. This means that after the kth iteration, the relative spectral error

$$\varepsilon_{(k)} = \frac{\left\|\Lambda_{(k)} - \Lambda_{\text{meas}}\right\|_2}{\left\|\Lambda_{\text{meas}}\right\|_2}$$

can be calculated, where Λ_{meas} is the measured ND map and $\Lambda_{(k)}$ is the computed ND map of the kth iteration for the CEM. For the $k+1$st iteration, we can thus generate an adaptive mesh of approximate sensitivity

$$\lambda_\sigma = \min\left\{\alpha \cdot \varepsilon_{(k)}, \ \beta\right\}, \quad \alpha \in (0, 1), \quad \beta > 0,$$

to account for the successive refinement of reconstructed details. Then we interpolate the conductivity of the current iteration on the new mesh for the next iteration. This dynamic refinement is particularly helpful for generating meshes when the spectral error level of the measured data is unknown.

In our tests, we choose $\alpha = 0.8$, $\beta = 0.05$ and only generate a new mesh in the k_lth iteration if the relative spectral error decreased sufficiently, i.e. if $\varepsilon_{(k_l)} \leq \alpha \cdot \varepsilon_{(k_{l-1})}$, where k_{l-1} is the last iteration where an adaptive mesh was generated. The dynamic refinement during the reconstruction of a conducting inclusion is shown in Figure 7.
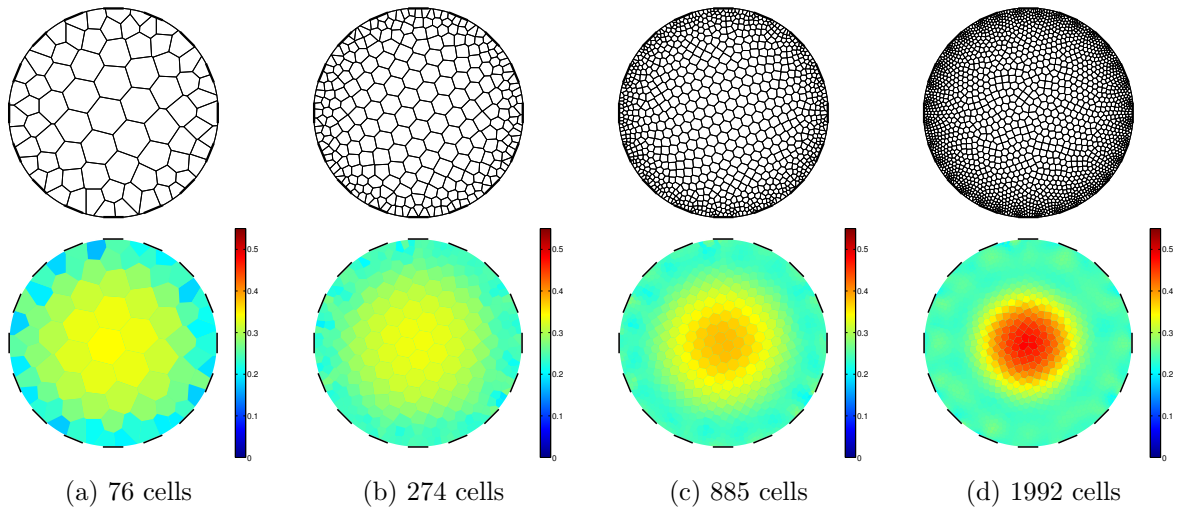
(a) 76 cells   (b) 274 cells   (c) 885 cells   (d) 1992 cells

FIGURE 7. Adaptive meshes generated during inversion, see Figure 8d.

6. NUMERICAL RESULTS

In this section we present the performance of optimal resolution meshes and its adaptive approximations for the reconstruction of EIT images. The algorithm used is the regularized inexact Newton method REGINN described in [Rie99] and applied to EIT in [LR06]. In the conjugate gradient iteration of REGINN, we use the Euclidean inner product on $\mathbb{R}^n$ for the discrete conductivity space instead of the area-dependent L^2 inner product used in [LR06]. This is because by design, the impact of each conductivity segment to measured data is roughly the same, independent of its area.

When adding artificial noise of level $\delta > 0$ to potential vectors $U \in \mathbb{R}^L$ from simulated data, we mean component-wise relative noise

$$U_{\text{noisy}} = U + \gamma \left(n_1 U_1, \, \dots, n_L U_L \right)^{\top},$$

where $n \in [-1, 1]^L$ is uniformly distributed noise and $\gamma > 0$ is chosen such that

$$\|U_{\text{noisy}} - U\|_2 = \delta.$$

Note that this does not necessarily result in a relative spectral error ε of the ND map of the same value. The relative error between the reconstructed conductivity σ_{rec} and the exact solution σ is computed as

$$e = \frac{\|P_\Delta \sigma_{\text{rec}} - P_\Delta \sigma\|_{L^2(\Delta)}}{\|P_\Delta \sigma\|_{L^2(\Delta)}},$$

where P_Δ is an interpolation on a very fine triangulation Δ of the domain Ω. Throughout all numerical simulations, we use $L = 16$ equally distributed electrodes that cover 50% of the boundary with contact impedances $z_l = 0.01 \frac{2\pi}{|\partial\Omega|}$, $l = 1, \dots, L$.

The REGINN parameters are $\mu_0 = 0.6$, $R = 1.02$ and $\zeta = 0.95$ in the notation of [LR06, section 6] which we found to be robust throughout all our experiments. Thus, the noise level is the only regularization parameter that needs to be specified when reconstructing from measured data.

We observed that the number of iterations until convergence, denoted by n_{it} in the following, significantly depends on the error level δ and the type of inclusions. For conducting inclusions and $\delta = 1\%$, we have $n_{\text{it}} \approx 5$–15. For resistive inclusions and $\delta = 0.2\%$, $n_{\text{it}} \approx 50$–100. Each iteration takes less than one second in MATLAB on an Intel i7 notebook.

6.1. **Reconstructions on the unit disk.** First, we reconstruct circular inclusions of conductivity $\sigma_0 = 0.5$ and radius $r_Q = 0.4$ inside the unit disk with background conductivity $\sigma_1 = 0.25$. As we assume the background conductivity to be unknown, the initial guess is $\sigma_{\text{init}} \equiv 0.4$ on Ω. To avoid inverse crime, the data Λ_σ are generated with the analytic forward solver of section 4. Figure 8 shows reconstructions with uniformly spaced meshes, optimal resolution meshes and adaptive meshes. The resolution-controlled meshes result in faster convergence and better reconstructions with significantly fewer artifacts than the uniformly spaced meshes.

| (a) True conductivity | (b) Uniform mesh, $\delta = 1\%$ noise | (c) Opt. res. mesh, $\delta = 1\%$ noise | (d) Adaptive mesh, $\delta = 0.2\%$ noise |

Top row: $n_{\text{it}} = 24$, $e = 25.0\%$; $n_{\text{it}} = 8$, $e = 21.8\%$; $n_{\text{it}} = 35$, $e = 15.2\%$

Bottom row: $n_{\text{it}} = 43$, $e = 19.0\%$; $n_{\text{it}} = 12$, $e = 17.0\%$; $n_{\text{it}} = 45$, $e = 13.3\%$
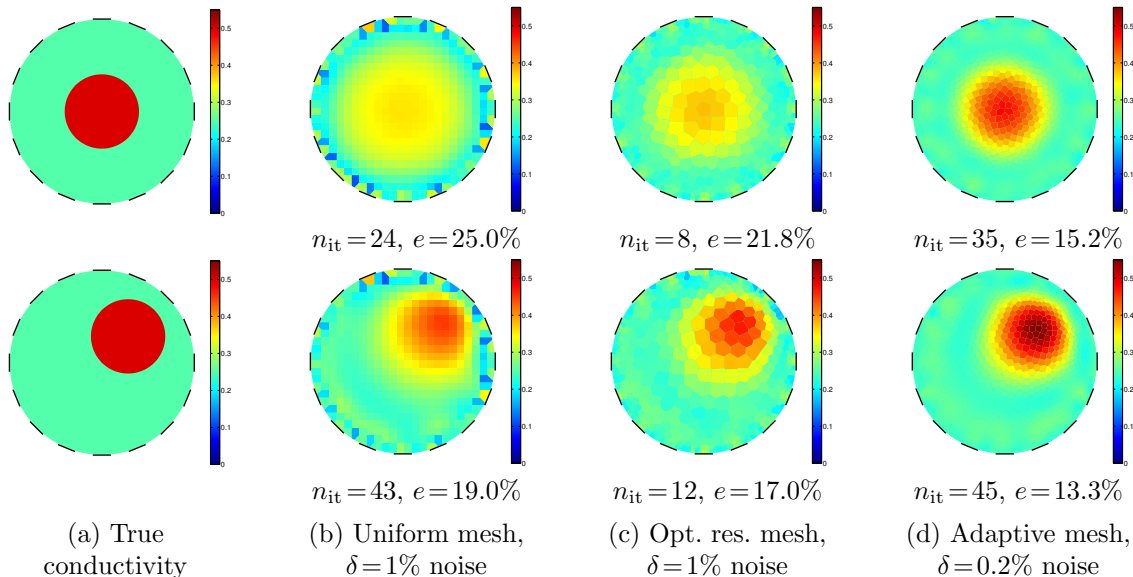
FIGURE 8. Settings with conducting inclusions and reconstructions from noisy data. The adaptive mesh was used for the very low noise level as the computation of an according optimal resolution mesh would be too computationally costly.

6.2. **Reconstructions on polygonal domains.** Next, we demonstrate the performance of adaptive meshes on non-circular domains. The simulated data are generated by finite elements on very fine triangle meshes. The initial guess for all settings is $\sigma_{\text{init}} \equiv 0.3$. The results are shown in Figure 9.

The first setting is a square with conductivity $\sigma = 0.25$, a conducting segment ($\sigma = 0.5$), a resistive segment ($\sigma = 0.1$) and $\delta = 1\%$ noise. The challenge of this setting are the jumps of conductivity in the interior and along the boundary.

The second setting is a chest-shaped domain with $\sigma = 0.25$, highly resistive inclusions ($\sigma = 0.05$), a conducting inclusion ($\sigma = 0.5$) and $\delta = 0.5\%$ noise. The small conductivity coefficient in large parts of the domain means a small ellipticity constant of the variational formulation, leading to slower convergence.

The third setting is an L-shaped domain with $\sigma = 0.25$, a conducting circular inclusion ($\sigma = 0.5$), a resistive annulus ($\sigma = 0.1$) and $\delta = 0.25\%$ noise.

6.3. **Reconstructions from measured data.** The measured data from a tank experiment were kindly provided by Aku Seppänen (University of Eastern Finland) and Stratos Staboulis (Aalto University). The tank has a circumference of 0.88m and a height of 7cm, each of the 16 electrodes has a width of 2.5cm. It is filled with saline ($0.016\,\Omega^{-1}m^{-1}$) and two conducting (metal) objects. The estimated measurement tolerance of the EIT equipment is $\delta \approx 0.1$–0.2%, but to account for the imperfections of the model and the contact impedances (we assume $z_l = 0.01\frac{2\pi}{|\partial\Omega|}$), we set $\delta = 0.3\%$ as the estimated measurement error for the REGINN algorithm.
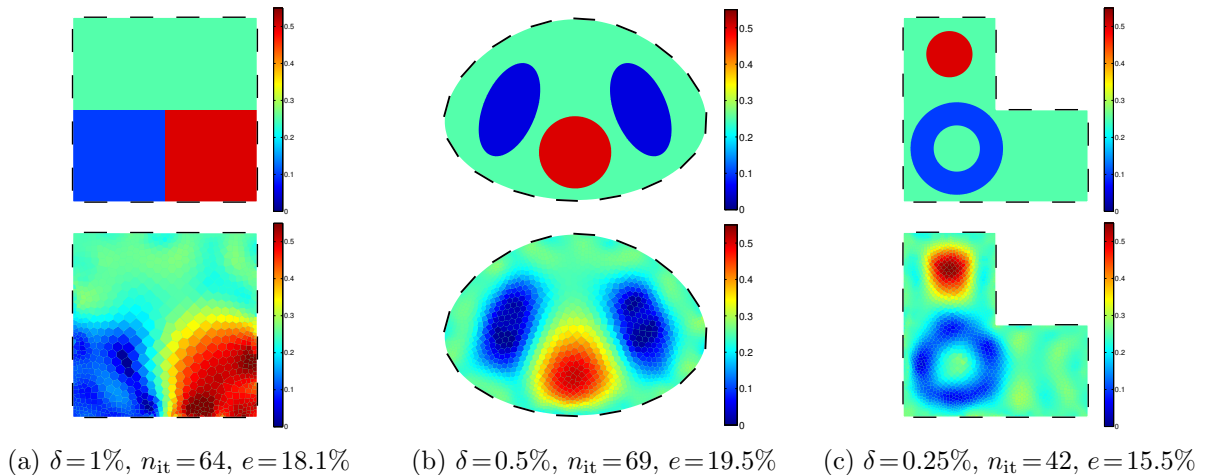
(a) $\delta = 1\%$, $n_{\mathrm{it}} = 64$, $e = 18.1\%$ (b) $\delta = 0.5\%$, $n_{\mathrm{it}} = 69$, $e = 19.5\%$ (c) $\delta = 0.25\%$, $n_{\mathrm{it}} = 42$, $e = 15.5\%$

FIGURE 9. Reconstructions from noisy simulated data with adaptive meshes.

The algorithm converges after $n_{\mathrm{it}} = 35$ iterations for $\sigma_{\mathrm{init}} = 0.3$. The resulting reconstruction is shown in Figure 10.
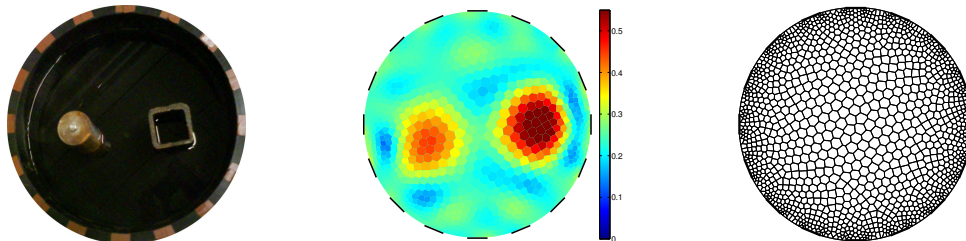

FIGURE 10. Measurement setting, reconstruction from measured tank data and the according adaptive mesh.

7. CONCLUSIONS

Using conformal maps, we introduced an analytic method to determine the sensitivity of boundary measurements to perturbations in conductivity for the CEM on circular domains. With this information, we determined the spatial resolution of various CEM settings and discretized the conductivity space accordingly, resulting in improved robustness and faster convergence when solving the ICP with Newton-type algorithms and noisy data.

Moreover, we pointed out the connections and differences of the CEM and the continuum boundary model in terms of imaging resolution.

Finally, we derived a heuristic approximation of sensitivity based discretizations of the conductivity space for non-circular domains and verified its performance with simulated and measured data.

8. ACKNOWLEDGEMENTS

Appendix A. Computing the analytic solution

Here we derive the formulas for the analytic forward solution of the CEM.

A.1. **Fourier representation of the potential for a centered perturbation.** We will express the potential $u = u(r, \theta)$ on Ω as a Fourier series in polar coordinates. The potential u can be split in even and odd parts in θ and each part can be treated separately, hence assume first that u is even in θ. According to [SCI92, (A3.4)], u is of the form

$$u(r, \theta) = u_0 + \begin{cases} \displaystyle\sum_{k=1}^{\infty} \left(\frac{r}{r_0}\right)^k a_k^{(1)} \cos(k\theta), & r \le r_0, \\ \displaystyle\sum_{k=1}^{\infty} \left(r^{-k} a_k^{(2)} + r^k a_k^{(3)}\right) \cos(k\theta), & r_0 \le r < 1, \end{cases}$$

for some coefficients $a_k^{(1,2,3)} \in \mathbb{R}$. By matching u and $\sigma \partial u / \partial r$ at $r = r_0$, we find from the orthogonality of the Fourier basis that

$$a_k^{(1)} = a_k^{(3)} r_0^k + a_k^{(2)} r_0^{-k} \quad \text{(condition on } u) \quad \text{and}$$

$$\sigma_0 a_k^{(1)} = \sigma_1 \left(a_k^{(3)} r_0^k - a_k^{(2)} r_0^{-k}\right) \quad \text{(condition on } \sigma \partial u / \partial r).$$

Substituting the first into the second equation, we get

$$a_k^{(2)} = c_k a_k^{(3)} \quad \text{with} \quad c_k := \frac{\sigma_1/\sigma_0 - 1}{\sigma_1/\sigma_0 + 1} r_0^{2k},$$

thus outside the perturbation, u has the representation

$$u(r, \theta) = u_0 + \sum_{k=1}^{\infty} \left(r^k + r^{-k} c_k\right) a_k^{(3)} \cos(k\theta),$$

$$\frac{\partial u}{\partial r}(r, \theta) = \sum_{k=1}^{\infty} k \left(r^{k-1} - r^{-k-1} c_k\right) a_k^{(3)} \cos(k\theta).$$

By evaluating u at $r = 1$ and letting $a_k := (1 + c_k) a_k^{(3)}$, we can express the potential and normal current at the boundary as

$$u(1, \theta) = u_0 + \sum_{k=1}^{\infty} a_k \cos(k\theta),$$

$$\sigma_1 \frac{\partial u}{\partial r}(1, \theta) = \sigma_1 \sum_{k=1}^{\infty} d_k \, a_k \cos(k\theta), \quad \text{where} \quad d_k := k \frac{1 - c_k}{1 + c_k}.$$

For the odd part of u in θ we can do the same calculations, replacing the cosine terms by sine terms and introducing coefficients b_k. Combining both, we get the desired representations (10).

A.2. **Computation of the Fourier coefficients for given electrode potentials.** We now apply the approach of [Dem11, Appendix] to (10) to determine the Fourier coefficients u_0 and a_k, b_k, $k \in \mathbb{N}$, therein for a given voltage pattern $U = (U_1, \ldots, U_L)^\top$ in the CEM. To that end, we rewrite (4b) as $i_\nu = \frac{1}{z_l}(U_l - u)$ and plug in the representations (10) for u and i_ν which yields

$$
(24) \qquad
\begin{aligned}
&\sigma_1 \sum_{k=1}^{\infty} d_k \left(a_k \cos(k\theta) + b_k \sin(k\theta)\right) \\
&\quad = \begin{cases} \frac{1}{z_l}\left(U_l - u_0 - \sum_{k=1}^{\infty} a_k \cos(k\theta) + b_k \sin(k\theta)\right) & \text{on } E_l, \ l = 1, \ldots, L, \\ 0, & \text{otherwise.} \end{cases}
\end{aligned}
$$

Following the idea of [Dem11, Appendix], we multiply (24) with

$$\cos(n\theta), \quad n \in \mathbb{N}_0, \quad \text{and} \quad \sin(n\theta), \quad n \in \mathbb{N},$$

respectively and integrate in θ over $[0, 2\pi]$ which leads to the set of equations

$$
\begin{aligned}
0 = & \sum_{l=1}^{L} \frac{U_l - u_0}{z_l} 2\omega_l \\
& - \sum_{k=1}^{\infty} \frac{a_k}{z_l} \int_{\theta_l - \omega_l}^{\theta_l + \omega_l} \cos(k\theta)\, \mathrm{d}\theta + \frac{b_k}{z_l} \int_{\theta_l - \omega_l}^{\theta_l + \omega_l} \sin(k\theta)\, \mathrm{d}\theta \qquad \text{for } n = 0,
\end{aligned}
$$

$$(25)$$
$$
\begin{aligned}
\sigma_1 \pi d_n a_n = & \sum_{l=1}^{L} \frac{U_l - u_0}{z_l} \int_{\theta_l - \omega_l}^{\theta_l + \omega_l} \cos(n\theta)\, \mathrm{d}\theta \\
& - \sum_{k=1}^{\infty} \frac{a_k}{z_l} \int_{\theta_l - \omega_l}^{\theta_l + \omega_l} \cos(n\theta)\cos(k\theta)\, \mathrm{d}\theta + \frac{b_k}{z_l} \int_{\theta_l - \omega_l}^{\theta_l + \omega_l} \cos(n\theta)\sin(k\theta)\, \mathrm{d}\theta, \ n \in \mathbb{N},
\end{aligned}
$$

$$
\begin{aligned}
\sigma_1 \pi d_n b_n = & \sum_{l=1}^{L} \frac{U_l - u_0}{z_l} \int_{\theta_l - \omega_l}^{\theta_l + \omega_l} \sin(n\theta)\, \mathrm{d}\theta \\
& - \sum_{k=1}^{\infty} \frac{a_k}{z_l} \int_{\theta_l - \omega_l}^{\theta_l + \omega_l} \sin(n\theta)\cos(k\theta)\, \mathrm{d}\theta + \frac{b_k}{z_l} \int_{\theta_l - \omega_l}^{\theta_l + \omega_l} \sin(n\theta)\sin(k\theta)\, \mathrm{d}\theta, \ n \in \mathbb{N},
\end{aligned}
$$

where $\theta_l \in [0, 2\pi)$ is the angular coordinate of the lth electrode center and $\omega_l > 0$ is its angular half-width. These equations can be rewritten as an infinite system of linear equations for u_0, a_k, b_k as

$$(26) \qquad \begin{pmatrix} r^U \\ s^U \end{pmatrix} = \begin{pmatrix} A & B \\ B^\top & C \end{pmatrix} (u_0, a_1, a_2, \ldots, b_1, b_2, \ldots)^\top,$$

with the (infinite dimensional) vectors

$$r^U = \left(r_0^U, r_1^U, \ldots \right)^\top, \quad s^U = \left(s_1^U, s_2^U, \ldots \right)^\top$$

and matrices

$$
A = \begin{pmatrix} A_{00} & A_{01} & \cdots \\ A_{10} & A_{11} & \cdots \\ \vdots & \vdots & \ddots \end{pmatrix}, \quad
B = \begin{pmatrix} B_{01} & B_{02} & \cdots \\ B_{11} & B_{12} & \cdots \\ \vdots & \vdots & \ddots \end{pmatrix}, \quad
C = \begin{pmatrix} C_{11} & C_{12} & \cdots \\ C_{21} & C_{22} & \cdots \\ \vdots & \vdots & \ddots \end{pmatrix}
$$

with entries

$$(27) \qquad A_{nk} = \sum_{l=1}^{L} \frac{1}{z_l} \underbrace{\int_{\theta_l - \omega_l}^{\theta_l + \omega_l} \cos(n\theta)\cos(k\theta)\, \mathrm{d}\theta}_{= \frac{1}{2}[s_l(k-n) + s_l(k+n)]} + \delta_{nk}\sigma_1 \pi d_k, \qquad n \in \mathbb{N}_0, \ k \in \mathbb{N}_0,$$

$$B_{nk} = \sum_{l=1}^{L} \frac{1}{z_l} \underbrace{\int_{\theta_l - \omega_l}^{\theta_l + \omega_l} \cos(n\theta)\sin(k\theta)\, \mathrm{d}\theta}_{= -\frac{1}{2}[c_l(k-n) + c_l(k+n)]}, \qquad n \in \mathbb{N}_0, \ k \in \mathbb{N},$$

$$C_{nk} = \sum_{l=1}^{L} \frac{1}{z_l} \underbrace{\int_{\theta_l - \omega_l}^{\theta_l + \omega_l} \sin(n\theta)\sin(k\theta)\, \mathrm{d}\theta}_{= \frac{1}{2}[s_l(k-n) - s_l(k+n)]} + \delta_{nk}\sigma_1 \pi d_k, \qquad n \in \mathbb{N}, \ k \in \mathbb{N},$$

$$r_n^U = \sum_{l=1}^L \frac{U_l}{z_l} \underbrace{\int_{\theta_l - \omega_l}^{\theta_l + \omega_l} \cos(n\theta)\,\mathrm{d}\theta}_{=s_l(n)}, \qquad\qquad n \in \mathbb{N}_0,$$

$$s_n^U = \sum_{l=1}^L \frac{U_l}{z_l} \underbrace{\int_{\theta_l - \omega_l}^{\theta_l + \omega_l} \sin(n\theta)\,\mathrm{d}\theta}_{=-c_l(n)}, \qquad\qquad n \in \mathbb{N},$$

where δ_{nk} is the Kronecker delta. Above integrals have analytic solutions given by the expressions s_l and c_l, where $s_l(0) = 2\omega_l$, $c_l(0) = 0$ and

$$s_l(n) = \tfrac{\sin(n(\theta_l + \omega_l)) - \sin(n(\theta_l - \omega_l))}{n}, \ c_l(n) = \tfrac{\cos(n(\theta_l + \omega_l)) - \cos(n(\theta_l - \omega_l))}{n}, \ n \in \mathbb{Z} \setminus \{0\}\,.$$

Once the Fourier coefficients are known, we can compute the lth entry of the resulting current vector I by (4c), integrating the left-hand side of (24) over the lth electrode:

$$I_l = \int_{E_l} i_\nu \,\mathrm{d}S = \sigma_1 \sum_{k=1}^\infty d_k \left(a_k s_l(k) - b_k c_l(k)\right).$$

However, it is advisable to integrate over the faster converging Fourier series on the right-hand side of (24) which yields

$$I_l = \frac{1}{z_l} \left(2\omega_l(U_l - u_0) - \sum_{k=1}^\infty a_k s_l(k) - b_k c_l(k) \right).$$

Remark: In practice, we truncate the Fourier series to get a finite system of linear equations. The truncation index N should be chosen with respect to the electrode widths such that the potential and normal current along all electrodes are approximated well by the truncated Fourier series. For example, if $2\omega_{\min}$ is the smallest electrode angular width, the truncation index should be chosen well above the "critical" index $\lceil 2\pi/(2\omega_{\min})\rceil$ of a Fourier sum that can resolve details of size $2\omega_{\min}$. In our implementations, we found $N = \max\{\lceil 32\pi/\omega_{\min}\rceil, 1000\}$ to give results of very high accuracy.

Appendix B. Analytic solution for the CEM forward problem under conformal mapping

By the Riemann mapping theorem, any simply connected smooth domain can be mapped to the unit circle *conformally*, that is, angle-preserving [Neh52, SL91]. We use conformal maps to reduce non-concentric EIT geometries to the concentric circular case. In this simpler geometry, we can solve the forward problem in EIT analytically. We now derive the analytic solution for the transformed CEM forward problem, incorporating the non-constant contact impedances in the formulas of Appendix A.2. Since the reciprocal of the transformed conductivity given in (18) is unsuitable for analytic (closed form) integration when multiplied by cosine or sine terms, we rewrite equation (19b) to avoid a term of the form $\frac{1}{\cos(\vartheta)}$ on either side of the equation. To achieve this, we use the representation

$$(28) \qquad \frac{1 + R^2}{1 - R^2} i_\nu^w(\vartheta) = \begin{cases} \dfrac{1}{z_l}\left(U_l - f^w(\vartheta)\right) - \dfrac{2R\cos(\vartheta)}{1 - R^2} i_\nu^w(\vartheta) & \text{on } E_l^w, \\ 0 & \text{otherwise.} \end{cases}$$

As in the centered case, we multiply the Fourier representation of (28) with the test functions $\cos(n\vartheta)$, $n \in \mathbb{N}_0$, and $\sin(n\vartheta)$, $n \in \mathbb{N}$, respectively and integrate in ϑ over $[0, 2\pi]$. For better

readability, we write $\mathrm{t}\,(n\vartheta)$ for any of these test functions. On the left-hand side, we get

$$(29) \qquad \int_0^{2\pi} \mathrm{t}\,(n\vartheta)\frac{1+R^2}{1-R^2}i_\nu^w(\vartheta)\,\mathrm{d}\vartheta = \begin{cases} 0 & \text{for} \quad n=0, \\[2mm] \pi\sigma_1\dfrac{1+R^2}{1-R^2}d_n a_n & \text{for the cosine terms,} \\[2mm] \pi\sigma_1\dfrac{1+R^2}{1-R^2}d_n b_n & \text{for the sine terms.} \end{cases}$$

On the right-hand side, we get

$$\sum_{l=1}^L \frac{U_l}{z_l}\int_{\vartheta_l-v_l}^{\vartheta_l+v_l}\mathrm{t}\,(n\vartheta)\,\mathrm{d}\vartheta - u_0\sum_{l=1}^L\frac{1}{z_l}\int_{\vartheta_l-v_l}^{\vartheta_l+v_l}\mathrm{t}\,(n\vartheta)\,\mathrm{d}\vartheta$$

$$-\sum_{k=1}^\infty a_k\sum_{l=1}^L\left[\frac{1}{z_l}\int_{\vartheta_l-v_l}^{\vartheta_l+v_l}\mathrm{t}\,(n\vartheta)\cos(k\vartheta)\,\mathrm{d}\vartheta + \frac{2R\sigma_1 d_k}{1-R^2}\int_{\vartheta_l-v_l}^{\vartheta_l+v_l}\mathrm{t}\,(n\vartheta)\cos(\vartheta)\cos(k\vartheta)\,\mathrm{d}\vartheta\right]$$

$$-\sum_{k=1}^\infty b_k\sum_{l=1}^L\left[\frac{1}{z_l}\int_{\vartheta_l-v_l}^{\vartheta_l+v_l}\mathrm{t}\,(n\vartheta)\sin(k\vartheta)\,\mathrm{d}\vartheta + \frac{2R\sigma_1 d_k}{1-R^2}\int_{\vartheta_l-v_l}^{\vartheta_l+v_l}\mathrm{t}\,(n\vartheta)\cos(\vartheta)\sin(k\vartheta)\,\mathrm{d}\vartheta\right].$$

Now we rearrange each equation to be used as one row of a linear system of equations for u_0 and $a_k, b_k,\ k\in\mathbb{N}$, and return to the notation of (26). In the conformally mapped case, we get

$$(30) \qquad \begin{pmatrix} r^U \\ s^U \end{pmatrix} = \begin{pmatrix} A & B^1 \\ B^2 & C \end{pmatrix}\left(u_0, a_1, a_2, \ldots\, b_1, b_2, \ldots\right)^\top.$$

The matrix coefficients are

$$A_{nk} = \sum_{l=1}^L\frac{1}{z_l}\int_{\vartheta_l-v_l}^{\vartheta_l+v_l}\cos(n\vartheta)\cos(k\vartheta)\,\mathrm{d}\vartheta + \delta_{nk}\pi\sigma_1\frac{1+R^2}{1-R^2}d_k$$

$$\qquad + \frac{2R\sigma_1 d_k}{1-R^2}\sum_{l=1}^L\int_{\vartheta_l-v_l}^{\vartheta_l+v_l}\cos(n\vartheta)\cos(\vartheta)\cos(k\vartheta)\,\mathrm{d}\vartheta, \qquad\qquad n\in\mathbb{N}_0,\ k\in\mathbb{N}_0,$$

$$B_{nk}^1 = \sum_{l=1}^L\frac{1}{z_l}\int_{\vartheta_l-v_l}^{\vartheta_l+v_l}\cos(n\vartheta)\sin(k\vartheta)\,\mathrm{d}\vartheta$$

$$\qquad + \frac{2R\sigma_1 d_k}{1-R^2}\sum_{l=1}^L\int_{\vartheta_l-v_l}^{\vartheta_l+v_l}\cos(n\vartheta)\cos(\vartheta)\sin(k\vartheta)\,\mathrm{d}\vartheta, \qquad\qquad n\in\mathbb{N}_0,\ k\in\mathbb{N},$$

$$B_{nk}^2 = \sum_{l=1}^L\frac{1}{z_l}\int_{\vartheta_l-v_l}^{\vartheta_l+v_l}\sin(n\vartheta)\cos(k\vartheta)\,\mathrm{d}\vartheta$$

$$\qquad + \frac{2R\sigma_1 d_k}{1-R^2}\sum_{l=1}^L\int_{\vartheta_l-v_l}^{\vartheta_l+v_l}\sin(n\vartheta)\cos(\vartheta)\cos(k\vartheta)\,\mathrm{d}\vartheta, \qquad\qquad n\in\mathbb{N},\ k\in\mathbb{N}_0,$$

$$C_{nk} = \sum_{l=1}^L\frac{1}{z_l}\int_{\vartheta_l-v_l}^{\vartheta_l+v_l}\sin(n\vartheta)\sin(k\vartheta)\,\mathrm{d}\vartheta + \delta_{nk}\pi\sigma_1\frac{1+R^2}{1-R^2}d_k$$

$$\qquad + \frac{2R\sigma_1 d_k}{1-R^2}\sum_{l=1}^L\int_{\vartheta_l-v_l}^{\vartheta_l+v_l}\sin(n\vartheta)\cos(\vartheta)\sin(k\vartheta)\,\mathrm{d}\vartheta, \qquad\qquad n\in\mathbb{N},\ k\in\mathbb{N},$$

$$r_n = \sum_{l=1}^L\frac{U_l}{z_l}\int_{\vartheta_l-v_l}^{\vartheta_l+v_l}\cos(n\vartheta)\,\mathrm{d}\vartheta, \qquad\qquad\qquad\qquad n\in\mathbb{N}_0,$$

$$s_n = \sum_{l=1}^{L} \frac{U_l}{z_l} \int_{\vartheta_l - v_l}^{\vartheta_l + v_l} \sin(n\vartheta) \, d\vartheta. \qquad\qquad n \in \mathbb{N}.$$

Note in particular that $B_{nk}^1 \neq B_{kn}^2$ in general for $R > 0$ due to the influence of the coefficients d_k. In this representation, all integrals are given analytically by trigonometric identities. The integrals without the $\cos(\vartheta)$ factor match those of (27). The analytic solutions of the other integrals read

$$\frac{1}{4}\big[s_l(\alpha_{n,k}) + s_l(\beta_{n,k}) + s_l(\gamma_{n,k}) + s_l(\kappa_{n,k})\big] \qquad \text{in } A_{nk},$$

$$\frac{1}{4}\big[c_l(\alpha_{n,k}) + c_l(\beta_{n,k}) - c_l(\gamma_{n,k}) - c_l(\kappa_{n,k})\big] \qquad \text{in } B_{nk}^1 \text{ and } B_{kn}^2,$$

$$\frac{1}{4}\big[-s_l(\alpha_{n,k}) + s_l(\beta_{n,k}) + s_l(\gamma_{n,k}) - s_l(\kappa_{n,k})\big] \qquad \text{in } C_{nk},$$

where

$$\alpha_{n,k} = -k - n + 1, \quad \beta_{n,k} = -k + n + 1, \quad \gamma_{n,k} = k - n + 1, \quad \kappa_{n,k} = k + n + 1.$$

The solution of this system is the set of Fourier coefficients of the transformed Dirichlet data f^w. For the truncation and the computation of the current vector, the same comments apply as in Appendix A.2. In particular, it is advisable to integrate over the right-hand side of (28) which yields

$$I_l = \frac{1 - R^2}{(1 + R^2)z_l}\left(2\omega_l(U_l - u_0) - \sum_{k=1}^{\infty} a_k s_l(k) - b_k c_l(k)\right)$$

$$+ \frac{R\sigma_1}{1 + R^2}\sum_{k=1}^{\infty} d_k \big[a_k\left(s_l(k-1) + s_l(k+1)\right) - b_k\left(c_l(k-1) + c_l(k+1)\right)\big].$$

APPENDIX C. MONOTONY OF THE SENSITIVITY

This is a CEM version of [GIN90, Appendix I]. The energy functional

$$J(u, U) = \frac{1}{2}a\left((u, U), (u, U)\right) - \sum_{l=1}^{L} I_l U_l$$

for the bilinear operator a from (6) has the minimizing property

$$J(u^*, U^*) = \min_{(u,U) \in H^1(\Omega) \times \mathbb{R}^L} J(u, U),$$

where (u^*, U^*) is the solution of the CEM for current vector I. Denote by a_B and a_D the bilinear operators, by J_B and J_D the energy functionals and by (u_B, U_B) and (u_D, U_D) the CEM solutions for conductivities σ_B and σ_D from (12), respectively. Using (5), we immediately get

$$J_B(u_B, U_B) = -\frac{1}{2}I^\top U_B \quad \text{and} \quad J_D(u_D, U_D) = -\frac{1}{2}I^\top U_D.$$

From $\sigma_D \geq \sigma_B$ on Ω, it follows that

$$J_D(u_D, U_D) - J_B(u_D, U_D) = \frac{1}{2}\int_\Omega (\sigma_D - \sigma_B)|\nabla u_D|^2 \, dx \geq 0.$$

Using the minimizing property for J_B, we get

$$-I^\top U_D = 2J_D(u_D, U_D) \geq 2J_B(u_D, U_D) \geq 2J_B(u_B, U_B) = -I^\top U_B.$$

In terms of ND maps, we have that $U_B = \Lambda_{\sigma_B} I$ and $U_D = \Lambda_{\sigma_D} I$, thus

$$\langle I, (\Lambda_{\sigma_D} - \Lambda_{\sigma_B})I \rangle \leq 0$$

for all $0 \neq I \in \mathbb{R}^L_\diamond$. Similarly, we get

$$\langle I, (\Lambda_{\sigma_D} - \Lambda_{\sigma_1})I \rangle \leq 0 \quad \text{and} \quad \langle I, (\Lambda_{\sigma_B} - \Lambda_{\sigma_1})I \rangle \leq 0$$

and finally $\langle I, (\Lambda_{\sigma_D} - \Lambda_{\sigma_1})I \rangle \leq \langle I, (\Lambda_{\sigma_B} - \Lambda_{\sigma_1})I \rangle \leq 0$, hence $\lambda_{\sigma_D, \sigma_1} \geq \lambda_{\sigma_B, \sigma_1}$.

References

[Ale88]   G Alessandrini. Stable determination of conductivity by boundary measurements. *Applicable Analysis*, 27(1-3):153–172, 1988.

[AP06]   K Astala and L Päivärinta. Calderón's inverse conductivity problem in the plane. *Annals of Mathematics*, pages 265–299, 2006.

[BDGVM12]   L Borcea, V Druskin, F Guevara Vasquez, and AV Mamonov. *Inverse Problems and Applications: Inside Out II*, volume 60, chapter Resistor network approaches to electrical impedance tomography, pages 55–118. Cambridge University Press, 2012.

[BH00]   M Brühl and M Hanke. Numerical implementation of two noniterative methods for locating inclusions by impedance tomography. *Inverse Problems*, 16(4):1029–1042, 2000.

[Cal80]   AP Calderón. On an inverse boundary value problem. In *Seminar on Numerical Analysis and its Applications to Continuum Physics*, pages 65–73. Soc. Brasileira de Matemática, 1980.

[CM00]   EB Curtis and JA Morrow. *Inverse problems for electrical networks*, volume 13. World Scientific, 2000.

[Dem11]   E Demidenko. An analytic solution to the homogeneous eit problem on the 2d disk and its application to estimation of electrode contact impedances. *Physiological Measurement*, 32(9):1453–1471, 2011.

[DHH+12]   J Dardé, H Hakula, N Hyvönen, S Staboulis, and E Somersalo. Fine-tuning electrode information in electrical impedance tomography. *Inverse Problems and Imaging*, 6(3):399–421, 2012.

[DHSS13]   J Dardé, N Hyvönen, A Seppänen, and S Staboulis. Simultaneous reconstruction of outer boundary shape and admittivity distribution in electrical impedance tomography. *SIAM Journal on Imaging Sciences*, 6(1):176–198, 2013.

[Dob92]   DC Dobson. Estimates on resolution and stabilization for the linearized inverse conductivity problem. *Inverse problems*, 8(1):71–81, 1992.

[GIN90]   DG Gisser, D Isaacson, and JC Newell. Electric current computed tomography and eigenvalues. *SIAM Journal on Applied Mathematics*, 50(6):1623–1634, 1990.

[Isa86]   D Isaacson. Distinguishability of conductivities by electric current computed tomography. *Medical Imaging, IEEE Transactions on*, 5(2):91–95, 1986.

[LR06]   A Lechleiter and A Rieder. Newton regularizations for impedance tomography: a numerical study. *Inverse Problems*, 22(6):1967–1987, 2006.

[LR08]   A Lechleiter and A Rieder. Newton regularizations for impedance tomography: convergence by local injectivity. *Inverse Problems*, 24(6):065009, 2008.

[MMM04]   HR MacMillan, TA Manteuffel, and SF McCormick. First-order system least squares and electrical impedance tomography. *SIAM journal on numerical analysis*, 42(2):461–483, 2004.

[MS12]   JL Mueller and S Siltanen. *Linear and Nonlinear Inverse Problems with Practical Applications*, volume 10 of *Computational Science and Engineering*. SIAM, 2012.

[Nac96]   AI Nachman. Global uniqueness for a two-dimensional inverse boundary value problem. *Annals of Mathematics*, pages 71–96, 1996.

[Neh52]   Z Nehari. *Conformal mapping. 1952*, volume 13. 1952.

[Pal02]   VP Palamodov. Gabor analysis of the continuum model for impedance tomography. *Arkiv för Matematik*, 40(1):169–187, 2002.

[Rie99]   Andreas Rieder. On the regularization of nonlinear ill-posed problems via inexact newton iterations. *Inverse Problems*, 15(1):309–327, 1999.

[SCI92]   E Somersalo, M Cheney, and D Isaacson. Existence and uniqueness for electrode models for electric current computed tomography. *SIAM Journal on Applied Mathematics*, 52(4):1023–1040, 1992.

[SL91]   R Schinzinger and PAA Laura. *Conformal mapping: methods and applications*. Elsevier, Amsterdam, 1991.

[SYB84]   AD Seagar, TS Yeo, and RHT Bates. Full-wave computed tomography. part 2: Resolution limits. *IEE Proceedings A (Physical Science, Measurement and Instrumentation, Management and Education, Reviews)*, 131(8):616–622, 1984.

Institute for Applied and Numerical Mathematics,
Karlsruhe Institute for Technology, DE-76049 Karlsruhe, Germany.

IWRMM-Preprints seit 2012

Eine aktuelle Liste aller IWRMM-Preprints finden Sie auf:

www.math.kit.edu/iwrmm/seite/preprints